RSC Advances

ROYAL SOCIETY OF CHEMISTRY

www.rsc.org/advances

Cite this: DOI: 10.1039/c0xx00000x

www.rsc.org/xxxxxx

ARTICLE TYPE

Shape tailored $Ni_3(NO_3)_2(OH)_4$ nano-flakes simulating 3-D bouquet like structures for supercapacitors: Exploring the effect of electrolytes on stability and performance

Jickson Joseph, Ranjusha Rajagopalan[#], Anoop S.S, Amruthalakshmi V, Amrutha Ajay, Shantikumar V Nair, Avinash Balakrishnan*

Received (in XXX, XXX) Xth XXXXXXXXX 20XX, Accepted Xth XXXXXXXXX 20XX
DOI: 10.1039/b000000x

The present study demonstrates a novel, low temperature synthesis approach by which 3-D bouquets of nickel hydroxide nitrate were processed into high surface area electrodes for supercapacitor applications. The synthesized micro-bouquets comprised of randomly arrayed microporous nanoflakes (pore size: 2−6 nm) and exhibited a surface area of 150 m^2g^{-1}. Morphological evolution studies were done to elucidate how surface morphology of these electrode materials affect the redox reactions and hence the ultimate performance of the supercapacitor. The electrodes were tested in three different electrolytes namely lithium hydroxide, potassium hydroxide and sodium hydroxide. From the detailed electrochemical analysis, an intrinsic correlation between the capacitance, internal resistance and the surface morphology was deduced and explained on the basis of relative contributions from the faradaic properties in different electrolytes. Depending on the surface morphology and electrolyte incorporated, these nano/micro-hybrid electrodes exhibited specific mass capacitance value as high as 1380 ± 38 Fg^{-1}. Inductively coupled plasma-atomic emission spectroscopy was used to determine the electrode dissolution in the given electrolyte and the findings were co-related with the cycling stability. By employing this low cost electrode design, high stability (> 5000 cycles with no fading) was attained in lithium hydroxide electrolyte. Further, a working model supercapacitor in coin cell form is also shown exhibiting peak power and energy density of 3 $kWkg^{-1}$ and 800 $mWhkg^{-1}$ respectively.

Keywords: Electrochemical; supercapacitor; Nano; Micro; Nickel hydroxide nitrate

1. Introduction

Superior energy storage technologies based on inexhaustible and economical resources are needed in order to enhance sustainability, reduce pollution and keep fossil fuel prices lower.[1-3] Energy storage devices like supercapacitors have significant applications in electronic systems like power back-up, micro-devices, electrical vehicles, etc.[4,5] Supercapacitor that exhibits reversible faradaic reactions at the electrode surface is called as pseudocapacitor.[6,7] In many cases, pseudocapacitors have specific capacitance exceeding to that of electric double layer supercapacitors made of carbonaceous materials.[22] Transition metal oxides and hydroxides are the typical active pseudocapacitor electrode materials. As compared to carbon, employing transitional materials can often result in a compromise between the power performance and reversibility because the redox kinetics is limited by the ion mobility and electron transfer rates[11,12]. Due to these kinetics, even though most of these transitional metal oxides/hydroxides have theoretical capacitance values (>1000 F g^{-1}), the practical values obtained are much lower.[9,13] A partial solution to this problem is by using nanostructured materials. But the low capacitance values still persist for these transitional nanostructures at high C-rates. Thus efforts have been made to improve the performance of these pseudocapacitive materials through engineered meso/micro-porous structures which are compounded with more active sites for achieving high rate capability.[14] In spite of these efforts, a huge challenge still remains to search for a low-cost, stable and high performing pseudocapacitive electrode material with good rate capability. To address the above issue, herein, a novel electrode material design is investigated wherein micro-porous nanoflakes are randomly arrayed in three-dimensional (3D) fashion. The material studied is nickel hydroxide nitrate ($Ni_3(NO_3)_2(OH)_4$). From the electrochemical point of view, nickel hydroxide nitrate is advantageous as it offers a layered CdI_2 structure.[15] As sites of the OH^- are substituted by the NO_3^-, the interlayer spacing obtained in these materials is larger than nickel hydroxide.[10] Such large interlayer spacing can be beneficial from ion diffusion point of view and have been exploited in nickel–cadmium battery applications.[16] To the best of our knowledge there are only two major reports on utilizing nickel hydroxide

nitrate for pseudocapacitors. For instance, Liu et al.[10] employed ultrathin nickel hydroxide nitrate nanoflakes grown on ZnO nanowire as electrodes in a 1 M NaOH electrolyte for pseudo-capacitor applications where specific capacitance as high as 1310 F g^{-1} at a discharge current density of 15.7 A g^{-1} was attained. Though promising, the synthesis technique reported here is complicated and secondly the utilization of ZnO nanowire semiconductors can reduce the current collection (through electron recombination[17]) and hence the capacitance, further the contributions from transitional zinc oxide in the final performance of the electrode were not discussed and cannot be neglected. Thus from the structural point of view, there is a scope for realizing and improving the practical specific capacitance of this material. This was shown in the studies by Kong et al,[18] where by employing flower like morphology of nickel hydroxide nitrate in 2M KOH, higher specific capacitance of 2212.5 F g^{-1} was reported at ~1.5 A g^{-1} during the initial discharge. Approximately 30 % fading was observed at the end of 1000 cycles limiting its application. We believe this fading could be attributed to the electrode-electrolyte combination which was detrimental for the electrode structure causing dissolution. This has been shown in our present study. Further, the values reported by Kong et al., exceeded the theoretical specific capacitance of these materials (~1500 Fg^{-1}).[10] This could be attributed due to the fact that the authors were incorporating acetylene black and graphite as current collectors, thus the double layer storage contributions along with faradaic contributions could have added to their final specific capacitance values. Our previous studies have shown that for pseudocapacitors, the charge storage mechanism coming from double layer effect of carbon current collectors play a significant role in improving the final performance of the electrode system.[8,19-21] Therefore, inorder to understand the true potential of these materials, the present study employs an electrophoretic deposition technique to attain thin film coatings comprising of phase pure nickel hydroxide nitrate. Micro-bouquets of $Ni_3(NO_3)_2(OH)_4$ was synthesized by a hydrothermal method without addition of any surfactant. The surface morphology of the hybrid structure showed randomly oriented micro-porous flakes (pore size: 2−6 nm). The electrochemical properties of $Ni_3(NO_3)_2(OH)_4$ were investigated by means of cyclic voltammetry, constant current charge–discharge tests and electrochemical impedance spectroscopy. A specific capacitance value of ~1380 Fg^{-1} (2.3 Fcm^{-2}) was obtained. It is the first time that such high values have been reported at high discharge current density and the effects of different electrolytes are analyzed in detail for these materials. The present study also demonstrates the first results on the performance of these electrodes when employed in a fully functional coin cell supercapacitor.

2. Experimental

2.1. Synthesis of $Ni_3(NO_3)_2(OH)_4$ powders

All the chemicals used in the present study were of analytical grade obtained from Nice Chemicals, India. Firstly, 0.015 M of Ni $(NO_3)_3.6H_2O$ was completely dissolved in 32 mL of distilled water under constant stirring condition. To this solution, 0.015 M of urea was added and completely dissolved. 32 mL of methanol was incorporated to this solution mixture. This methanolic solution was stirred for 30 min. The obtained clear solution was autoclaved in a teflon lined container at 90 ºC for different time intervals ranging from 6 to 36 h. The resultant solution was centrifuged for 20 min and obtained precipitate was thoroughly washed with de-ionized water and oven dried in air at 60 ºC for 12 h.

2.2 Electrophoretic deposition and surface characterization

Morphology and phase analyses were performed using scanning electron microscopy (SEM, Model: JEOL, JSM - 6390LV), high resolution-transmission electron microscopy (HR-TEM, Model: JEOL, JEM-2100F), fourier transform infrared spectroscopy (FT-IR, Model: Thermo Nicolet, Avatar 370) and X-ray diffraction analyses (XRD, X'Pert PRO Analytical). The resultant powders were electrophoretically deposited onto a nickel substrate. For this an electrochemical setup comprising of nickel foil (1 cm X 2 cm X 0.2 mm) was used as a substrate (cathode) and platinum wire as an anode. Isopropanol solution was used as the electrolyte solvent. To this electrolyte, 14 mg of $Ni_3(NO_3)_2(OH)_4$ synthesized powders were dispersed uniformly under constant stirring. For each batch, the deposition was carried out at 36 V for 20 min at room temperature, resulting in a thin uniform porous layer of $Ni_3(NO_3)_2(OH)_4$. The atomic force microscopy (AFM, JEOL SPM 5200) was used to measure the active surface area of the deposited layer. Surface area measurements were carried out using a BET analyzer (Nova Quantachrome, USA).

2.3. Electrochemical Characterization

Cyclic voltammetry (CV) and constant current charge-discharge were performed to evaluate the capacitance. For the electrochemical studies, a three electrode setup consisting of electrophoretically deposited $Ni_3(NO_3)_2(OH)_4$, platinum and Ag/AgCl (3 M KCl filling solution) electrode were used as working, counter and reference electrode, respectively. Different electrolytes comprising of KOH, NaOH and LiOH in 1M concentrations were used.

3. Results and discussion

3.1. Phase and morphological analyses

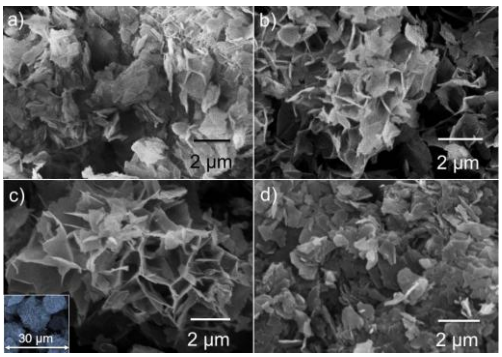

Fig. 1. SEM images displaying the morphology of synthesized $Ni_3(NO_3)_2(OH)_4$ hydrothermally at different times of (a) 6 h, (b) 12 h, (c) 24 h, and (d) 36 h.

Fig. 1(a–d) shows the SEM images displaying the morphology of hydrothermally synthesized $Ni_3(NO_3)_2(OH)_4$ powders at different processing times of 6, 12, 24 and 36 h hereby designated as N-6,

N-12, N-24 and N-36, respectively. It was observed that, as the processing time increases from 6 to 24 h the morphology changes from micro-clumps (Fig. 1(a&b)) to cluster of nano-flakes arrayed in spheroidal fashion (Fig. 1(c)). At the end of 24 h processing time N-24 samples showed microclusters with size ranging from 10-20 µm (see inset (Fig. 1(c)). As the processing time was increased to 36 h, N-36 samples showed clump like features similar to N-6 samples. This phenomenon can be mainly attributed to the agglomeration of the nanoflakes subjected to prolonged exposure of temperature and pressure during hydrothermal synthesis.

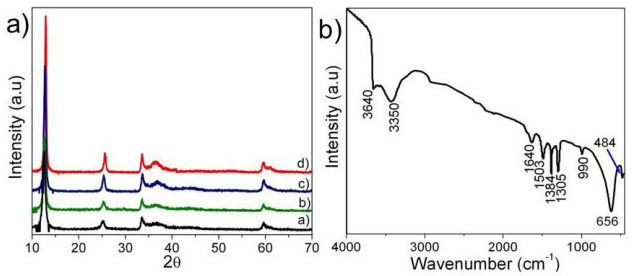

Fig. 2 a) XRD pattern b) FTIR spectrum of the synthesized $Ni_3(NO_3)_2(OH)_4$.

Fig. 2 (a) shows the typical XRD patterns of the synthesized powders where the diffraction peaks corresponded to pure phases of α- Ni_3 $(NO_3)_2(OH)_4$ (JCPDS 22-0752). It was seen that the crystallinity of the samples increased with the processing time. Fig. 2 (b) shows the typical FT-IR spectrum of as-prepared nickel nitrate hydroxide powders. Three peaks observed at 3640, 656, and 484 cm^{-1} correspond with the ν-OH stretching, σ-OH vibrations and ν-Ni–O vibration, respectively.[23,24] The vibrations of H_2O were manifested as two peaks at 3350 and 1640 cm^{-1}. The interlayer NO_3^- was observed as a set of strong peaks in the range of 1503 to 980 cm^{-1}. No vibrations of organic compounds (C–H vibration ~2900 cm^{-1})[23] were observed indicating the phase purity of the prepared powder. The effect of processing time was reflected in the surface area of the processed powder. Fig. 3 a represents the isotherm plots of synthesized samples; a surface area of 11, 14, 150 and 61 m^2g^{-1} was obtained for N-6, N-12, N-24 and N-36 samples, respectively.

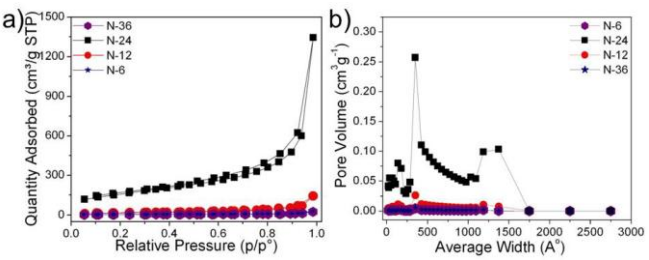

Fig. 3 a) Isotherm plots and b) pore size distribution plots of the of synthesized samples

Fig. 3 (b) shows pore size distributions for the synthesized powders. The pore size distributions of the N-24 samples were narrower and the pore diameters were smaller showing the presence of both micro and meso-pores. The pore diameters and pore volumes patterns of N-6, N-12 and N-36 illustrated that the prepared powders were non-porous nature which explained their low surface area (Fig. 3 (a)).

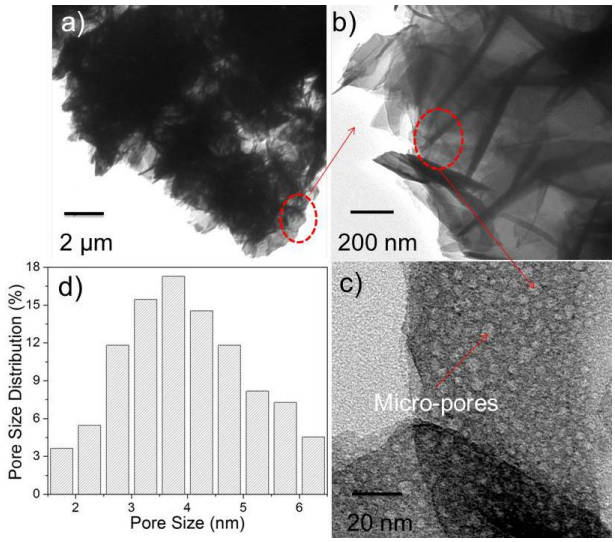

Fig. 4 (a -c) HR-TEM images of the nanoflakes and (d) pore size distribution

Fig.4 (a and b) shows the HR-TEM images and pore size distribution (Fig. 4(c)) of N-24 powders as obtained from TEM images (Fig. 4 (a-c)). The pore size varied from 2-8 nm. This micro/mesoporous nature of the N-24 sample is correlated with the high BET surface area value. The formation mechanism of α-Ni_3 $(NO_3)_2(OH)_4$ can be shown as follows:[25,26]

$$4CH_3OH + NO_3^- \leftrightarrow 4CH_2O + NH_3 + OH^- + 2H_2O \quad (I)$$

$$3Ni^{2+} + 4OH^- + 2NO_3^- \leftrightarrow - Ni_3(NO_3)_2(OH)_4 \quad (II)$$

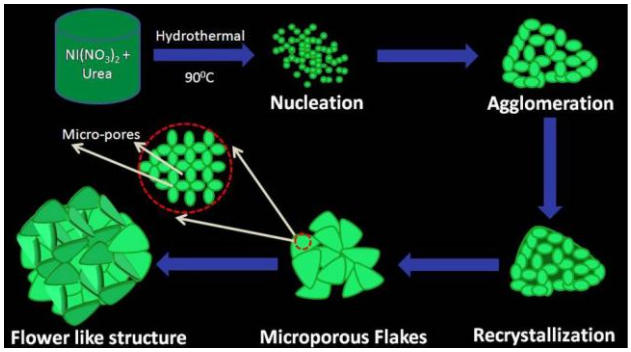

Fig. 5 The schematic representation of this formation mechanism of micro-porous $Ni_3(NO_3)_2(OH)_4$ 3-D structures

The initiation of flower like morphology starts with the nucleation of primary $Ni_3(NO_3)_2(OH)_4$ crystallites. As reported by Shinde et al.[27] as the ionic product exceeds the solubility product, positively charged and anisotropic $Ni_3(NO_3)_2(OH)_4$ nuclei are formed. This possibly occurs from homogeneous aqueous nickel nitrate solution due to intensive hydrolysis at elevated temperatures during hydrothermal process. As the reaction proceeds over a time period, these crystallites agglomerate/aggregate to self-organize themselves into micro-porous nanoflakes which self-assemble into 3-D structures. This self assembly of the flakes can be attributed to multiple factors such as electrostatic and dipolar fields associated with the agglomerations, hydrophobic interactions, hydrogen bonds, crystal face attraction and van der Waals forces of attraction.[28-30] In the present case, it is believed that the presence of functional

(nitrate and hydroxyl) groups, electrostatic interactions and hydrogen bonds have played a pivotal role in aiding the formation of flower like morphology.[24] The schematic representation of this formation mechanism of micro-porous $Ni_3(NO_3)_2(OH)_4$ 3-D structures is shown in Fig 5.

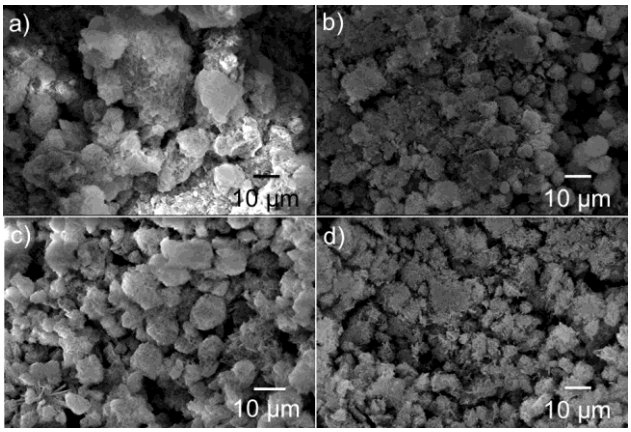

Fig. 6 SEM images of the electrophoretically deposited layer of a) N-6, b) N-12, c) N-24 and d) N-36 powders

Fig. 6(a-d) reveal the SEM images of the electrophoretically deposited layer of $Ni_3(NO_3)_2(OH)_4$ electrodes displaying a thickness of ~20-30 µm (see supporting information (SI)-I). All the powders seem to retain their initial morphology after electrophoretic deposition.

3.2. Electrochemical characterization

For a given electrolyte, all the fabricated electrodes (N-6, N-12, N-24 and N-36) showed similar redox patterns. Among all the electrodes, N-24 showed quite prominent redox peaks in the given electrolytes (Fig. 7(a-c)).

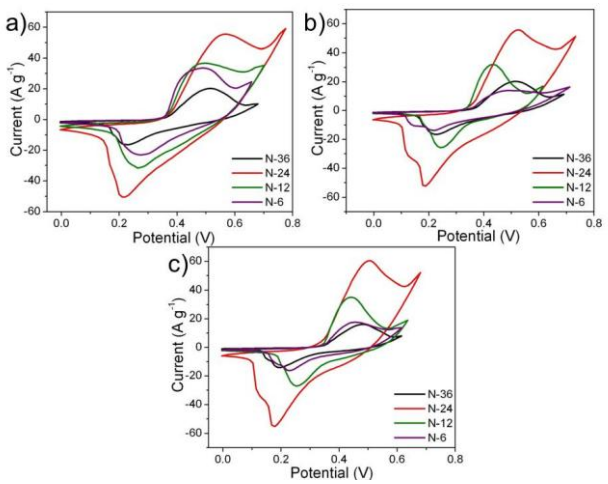

Fig. 7 CV curves of different electrodes in a) NaOH b) KOH and c) LiOH.

This seem to concur with the fact that N-24 powders showed higher surface area (see Fig. 3) where the 2D flake like structures make nickel nitrate hydroxide exclusively exposed to the electrolyte as compared to other electrode overlays. The mean surface roughness (R_a) for N-24 samples was measured using AFM and was found to be 0.150 µm (see SI-II). N-24 electrode showed similar performance in all the given electrolytes. Thus the further electrochemical characterization was done using N-24 electrodes.

3.2.3 Influence of CV scan rates

Fig. 8(a-c) shows the CV curves of N-24 electrode in LiOH, NaOH and KOH electrolytes at different scan rates. For all scan rates, a slight asymmetry in the redox pattern was observed indicating a pseudocapacitive like behavior. The mass specific capacitance was calculated using the following equation [34]:

$$C = \frac{1}{M \times \Delta V \times s} \times \int IdV \qquad (1)$$

where C is the mass specific capacitance (F g^{-1}), M is the mass of the active electrode, ΔV is the voltage window, s is the scan rate and I represents the current.

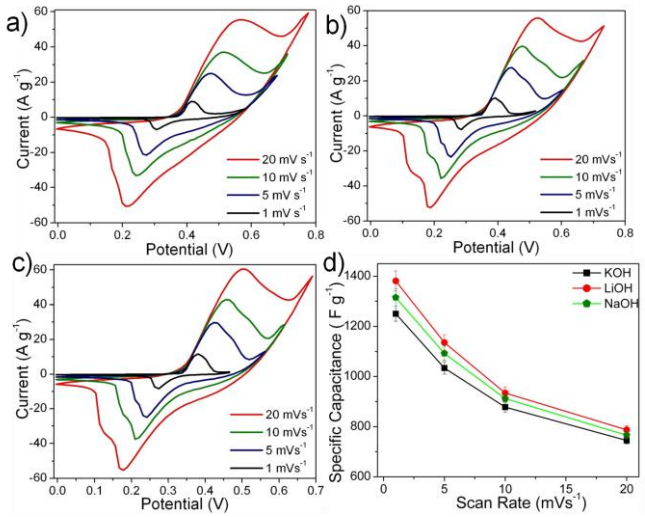

Fig. 8 CV curves of N-24 electrodes in a) LiOH, b) NaOH, and c) KOH electrolytes at different scan rates and d) plot showing the specific capacitance of N-24 electrodes calculated from these CV curves at different scan rates.

The redox peaks of $Ni_3(NO_3)_2(OH)_4$ electrodes (Fig. 8(a-c)) in the given electrolytes can be attributed to the intercalation and de-intercalation of OH^- ions from the electrolyte into the micro and/or mesopores of the flake like structure. The possible faradaic reactions occurring on the surface of $Ni_3(NO_3)_2(OH)_4$ can be shown as:

$$Ni_3(NO_3)_2(OH)_4 + yOH^- + e^- \leftrightarrow Ni_3(NO_3)_2(OH)_{4-y}.yOH^- + (1-y)\,Ni_3(NO_3)_2(OH)_4 + H_2O + e^- \quad (III)$$

At lower scan rates of 1 mVs^{-1}, the specific capacitance for LiOH, NaOH and KOH was found to be higher which implied more active sites participation as compared to 20 mV s^{-1} (Fig. 8(d)). This meant that by lowering the scan rate it is possible to increase OH^- intercalation–deintercalation reactions contributing an increase in the total capacitance of the electrode. The decrease in specific capacitance at faster scan rates can be attributed to the fact that the OH^- ions from the electrolyte reach only up to the electrode surface with limited entry into the deeper pores of the electrode.[31,32]

3.2.3 Cycling stability and internal resistance in different electrolytes

The cycling stability was determined using CV tests (scan rate: 50 mV s^{-1}) in different electrolytes and the area under the curve

was used to determine the specific capacitance of the electrodes (Fig. 9(a-c)). For the given electrode-electrolyte system the total number of cycles was determined for ~10 % capacitance fade. The best performance was observed in LiOH where the capacitance was found to be retained upto 8000 cycles (Fig. 9(a)). In NaOH system the capacitance fading was observed after 5000th cycle (Fig. 9(b)). Specific capacitance fading was observed to be faster in the KOH system (Fig. 9(c)) (at the end of 3000th cycle) as compared to other electrolytes. Similar trends were observed in all the three electrolyte systems i.e. initially an increase in capacitance value was observed and it retained for certain number of cycles and finally started fading after prolonged cycling (see Fig. 9(d)).

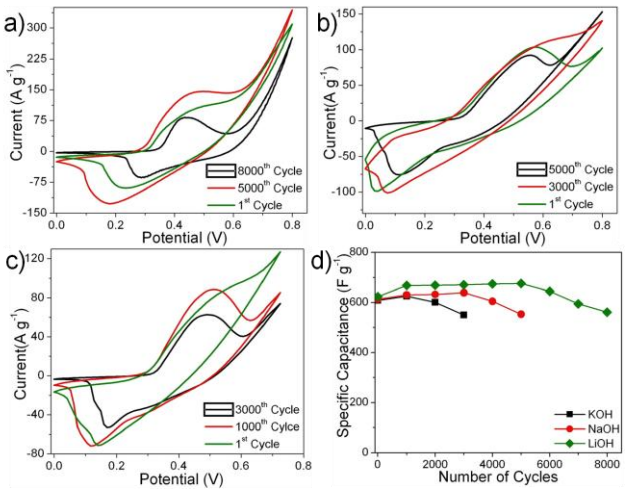

Fig. 9 CV curves of N-24 electrodes in a) LiOH, b) NaOH and c) KOH for different number of cycles. Scan rate: 50 mvs^{-1}

The initial increase in capacitance could be attributed to the pore opening phenomenon as observed in other metal oxide systems. The superior performance in LiOH could be attributed to the lower dissolution of nickel into the electrolyte.

Table 1: ICP-AES data for electrode dissolution in different electrolytes

	Electrolytes		
No. of cycles	LiOH	NaOH	KOH
1st	0.01	0.01	0.02
1000th	0.02	0.03	0.03
3000th	0.04	0.05	0.30
5000th	0.08	0.45	-
8000th	0.58	-	-

Values:In ppm

ICP-AES analysis of the electrolyte (see Table 1) at the end of 1st and last cycle showed lower dissolution of nickel in LiOH as compare to NaOH and KOH electrolyte systems.

Fig. 10(a) shows the Nyquist plots of N-24 electrodes in the three electrolytes. In the complex plane of the Nyquist plot, the imaginary component Z^{II} shows the capacitive nature and the real component Z^{I} shows the ohmic behavior. Both the components were studied in the frequency range of 0.1-10000 Hz. The Nyquist plots of a supercapacitor consist of three regions which are frequency dependent. At high frequencies, the supercapacitor exhibits pristine resistor behavior. The reactance (imaginary part) increases with decrease in frequency indicating a capacitive behavior. In the medium frequency domain, the influence of the electrode porosity can be observed.[36]

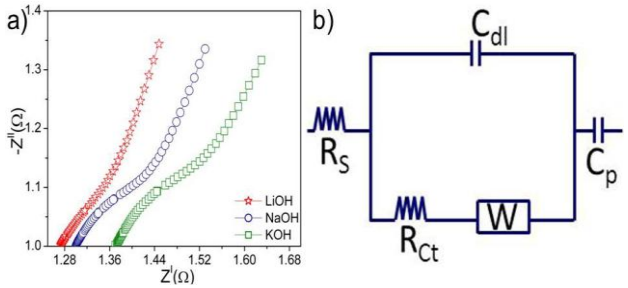

Fig. 10 a) Nyquist plots of N-24 electrodes in different electrolytes and b) Equivalent circuit obtained from the Nyquist plot.

As the frequency decreases from higher range to lower, the deeper pores of the electrode structure becomes available for ion adsorption.[41] The lower frequency region correspond to the the capacitive element of the electrode. The Warburg region lies in between the high frequency region and the low frequency region. This region is related to electrolyte penetration into the electrode pores.[42] In the present study, the EIS curves (Fig. 10(a)) corresponding to the three electrolyte systems showed linear behavior in the lower frequency region and an arc in the high frequency. The electrical resistance between the N-24 nanoflakes in a given electrolyte can be represented by R_s. It was observed that N-24 samples showed lower ohmic values in LiOH as compare to other two electrolytes. These shifts in the impedance spectra in the different electrolytes can be attributed to the effect of different cation size. For instance, in each electrolyte as OH^- ion intercalates in the anode, it is complemented by a cation tranfer at the counter electrode. Depending on the size; the cation density at the counter electrode/electrolyte interface will vary which is reflected in the ohmic values of the overall system. The higher the cation density at the electrolyte/electrode interface lower is the ohmic resistance. In the present case, Li^+ has lower ionic radius of 0.09 nm as compare to Na^+ (0.116 nm) and K^+ (0.152 nm).[22] Thus N-24 is anticipated to show lower ohmic values in LiOH as compare to the other electrolytes as shown in Fig. 10. The capacitive regions in case of LiOH were much more inclined indicating enhanced access of the electrolytic ions to the electrode surface. The equivalent series resistance (ESR) is observed from the x-intercept of the Nyquist plot. They are 1.27 Ω, 1.3 Ω and 1.37 Ω in LiOH, NaOH and KOH, respectively. The ESR data determine the rate at which the supercapacitor can be charged and discharged. It is a very important factor to determine the power density of a supercapacitor since the power density is inversely proportional to the ESR. The typical equivalent circuit corresponding to all these system is shown in Fig. 10(b). Considering the stability and lower ESR values N-24 electrodes in LiOH system was taken for further characterization.

3.2.4. Constant current discharge and self-discharge performance

Fig. 11(a) displays the constant current discharge performance of N-24 at different discharging currents. From these discharge curves, the capacitance, energy density and power density was derived using the following equations:[20]

$$C = \frac{I \times \Delta t}{m \times \Delta V} \quad (2)$$

$$E = \frac{1}{2}\frac{CV^2}{m} \quad (3)$$

$$P = \frac{V^2}{4R \times m} \quad (4)$$

Where C is the specific mass capacitance, I represent the discharge current, ΔV is the potential window and Δt is the total discharge time, V is the maximum voltage, E is the specific energy density, m is the mass of the active material and P is the specific power density, and R is the ESR.

The obtained specific capacitance values were 1380±38 F g^{-1} (2.3±.06Fcm^{-2}), 1162±32 F g^{-1}(1.94±.05 Fcm^{-2}), and 802±18 F g^{-1} (1.33± .03 Fcm^{-2}) at discharge current densities of 0.51 A g^{-1}, 5.1 A g^{-1}, and 51 A g^{-1}, respectively. It should be noted that the highest discharge current density i.e. 50 Ag^{-1} reported here is 3 times higher as compare to the discharge current density (~15.7 Ag^{-1}) reported by Liu et al[10] for the same

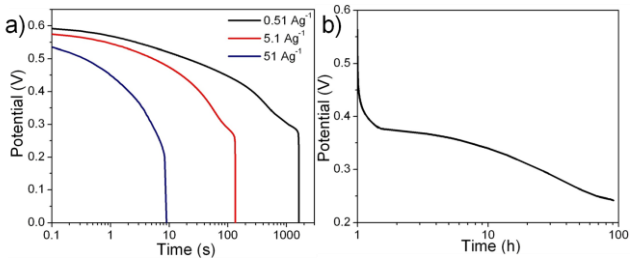

Fig. 11 a) Discharge curves of N-24 electrodes at different current densities and b) self-discharge behavior of N-24 electrodes in 1M LiOH.

material in 1 M KOH. The decrease in capacitance with the increase in applied current density is a quite known phenomenon for transition materials. The fading of specific capacitance at higher current densities can be attributed to different factors, like voltage (IR) drop, non-uniformly distributed pore resistance and severe redox reactions at the electrode surface.[33,34] The obtained energy and power density values for these N-24 electrodes in LiOH electrolyte were observed to be 56 Wh kg^{-1} and 27 kW kg^{-1}, respectively. The deviation in the linearity for the discharge curve corresponds to the redox behavior as observed in the CV curves (Fig. 8(a)) indicating a tendency towards battery like behavior.[40] Unlike battery this system showed high cycling stability (Fig. 9).The deviation during the discharge process could be attributed to multiple factors: a) variation in the direct equivalent series resistance, b) the redistribution of charge within the pores of the material structure and c) the pseudocapacitive behavior of the material.[36-39] However, identifying role of individual influences of the above mentioned factors on the electrode's performance is difficult and is beyond the scope of the present work. Fig. 11(b) shows the self-discharge behavior for period of ~100 h, where the total discharge was found to be ~50 %, indicating low self-discharge property.

As a preliminary study, the application of these N-24 electrodes was explored in a fully functional CR2032 coin cell (Fig. 12 (a)). Fig. 12 (b) shows a typical CR2032 coin cell. Fig. 12 (c) shows the discharge curves at 5, 25, 50 mAg^{-1}. A capacitance of ~15 mF at a peak voltage of ~1.75 V was obtained. The obtained peak energy and peak power density values for the coin cells were found to be ~ 800 $mWhkg^{-1}$ and 3 $kWkg^{-1}$, respectively. These samples showed good shelf life retaining their discharge capacitance even after 30 days.

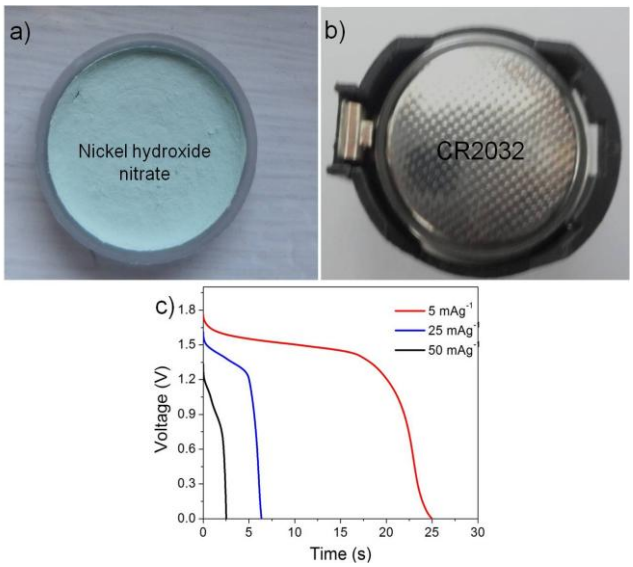

Fig.12 a) and b) Assembled button cell using N-24 electrode, c) discharge curve at different discharge currents

Although these results seems to be promising, the main conclusion of this investigation can only be validated once the performances of these N-24 electrodes are evaluated at higher and lower temperatures for different discharging currents. This work is currently been pursued by our group.

4. Conclusions

In summary, the present study investigates the performance of $Ni_3(NO_3)_2(OH)_4$ micro-bouquets for pseudocapacitor electrode applications. The presence of micro-pores on the $Ni_3(NO_3)_2(OH)_4$ nano-flakes has shown to increase the surface area. This porous electrode morphology shows advantages especially from higher mass specific capacitance (1380±38 Fg^{-1}) stand point with low self-discharge behaviour. The superior performance of these electrodes in conjunction with their reduced cost and low temperature fabrication makes them promising systems for pseudocapacitor applications.

Acknowledgements

Department of Science and Technology (DST), Government of India is gratefully acknowledged for their financial support to Dr Avinash Balakrishnan under Fast Track Scientist scheme. Ministry of New and Renewable Energy (MNRE), India is also acknowledged for their infrastructural support.

Notes and references

Nanosolar division, Amrita Center for Nanosciences, Kochi, India-682041. Tel: +91-484-2801234; E-mail: avinash.balakrishnan@gmail.com ,rranjusha@gmail.com

† Electronic Supplementary Information (ESI) available: [SEM & AFM image of material coated on nickel substrate]. See DOI: 10.1039/b000000x/

1 M. S. Whittingham, *Chem. Rev.*,2004, **104,** 4271.
2 A. Hochbaum and P. Yang, *Chem. Rev.*, 2010, **110,** 527.
3 J. R. Miller and P. Simon, *Science*, 2008, **321,** 651.
4 L. Cao, F. Xu, Y.Y. Liang and H.L. Li, *Adv. Mater.*, 2004, **16,** 1853.
5 D.D. Zhao, W.J. Zhou and H.L. Li, *Chem. Mater.*, 2007, **19,** 3882.
6 L.B. Kong, M.C. Liu, J.W. Lang, M. Liu, Y.C. Luo and L. Kang, *J. Solid State Electrochem.*, 2011, **15,** 571.
7 S.C. Pang, M.A. Anderson and T.W. Chapman, *J. Electrochem. Soc.*, 2000, **147,** 444.
8 R. Ranjusha, V. Prathibha, S. Ramakrishna, A. Sreekumaran Nair, P. Anjali, K.R.V. Subramanian, N. Sivakumar, T.N. Kim, S.V. Nair and A. Balakrishnan, *Scr. Mater.*, 2013, **68,** 881.
9 S. Roshny, R. Ranjusha, M. S. Deepak, N. Sanoj Rejinold, R. Jayakumar, S. V. Nair and A. Balakrishnan, *RSC Adv.*, 2014, **4,** 15863.
10 J. Liu, C. Cheng, W. Zhou, H. Li and H. J. Fan, *Chem. Commun.*, 2011, **47,** 3436.
11 R. Liu and S. B. Lee, *J. Am. Chem. Soc.*, 2008, **130,** 2942.
12 H. Pang, Q. Y. Lu, Y. Z. Zhang, Y. C. Li and F. Gao, *Nanoscale*, 2010, **2,** 920.
13 L. Gao, F. Xu, Y. Y. Liang and H. L. Li, *Adv. Mater.*, 2004, **16,** 1853.
14 R. Ranjusha, K.M. Sajesh, S. Roshny, V. Lakshmi, P. Anjali, T.S. Sonia, A. Sreekumaran Nair, K.R.V. Subramanian, Shantikumar V. Nair, K.P. Chennazhi and A. Balakrishnan, *Microporous Mesoporous Mater.*, 2014, **186,** 30.
15 J.Y. Miao, M. Xue, H. Itoh andQ. Feng, *J. Mater. Chem.*, 2005, **16,** 474.
16 D. Louer, *J. Mater. Sci.*,1985, **20,** 3729.
17 R. Ranjusha, P. Lekha, K.R.V. Subramanian, Shantikumar V. Nair, A. Balakrishnan, *J. Mater. Sci. Technol.*, 2011, **27,** 961.
18 L. B. Kong, L. Deng, X. M. Li, M. C. Liu, Y. C. Luo and L. Kang, *Mater. Res. Bull.*, 2012, **47,** 16411.
19 P. Anjali, A. S. Nair, R. Ranjusha, P. Praveen, K. R. V. Subramanian, N. Sivakumar, S. V. Nair and A. Balakrishnan, *ChemPlusChem*, 2013, **78,** 1258.
20 R. Ranjusha, S. Ramakrishna, A. S. Nair, P. Anjali, S. Vineeth, T. S. Sonia, N. Sivakumar, K. R. V. Subramanian, Shantikumar V. Nair and A. Balakrishnan, *RSC Adv.*, 2013, **3,** 17492.
21 T. S. Sonia, S. Roshny, R. Ranjusha, P. Anjali, V. Lakshmi, K. R. V. Subramanian, S. V. Nair and A. Balakrishnan, *RSC Adv.*, 2014, **4,** 11673.
22 R. Ranjusha, A. S. Nair, S. Ramakrishna, P. Anjali, K. Sujith, K. R. V. Subramanian, N. Sivakumar, T. N. Kim, S. V. Nair and A. Balakrishnan, *J. Mater. Chem*, 2012, **22,** 20465.
23 M. Taibi, S. Ammar, N. Jouini, F. Fie´vet, P. Molinie´ and M. Drillon, *J. Mater. Chem.*, 2002, **12,** 3238.
24 B. H. Liu, S. H. Yu, S. F. Chen, C. Y. Wu, *J. Phys. Chem. B* 2006, **110,** 4039.
25 C. Tang, G. Li, and L. Li, *Chemistry Letters*, 2008, **37,** 1138.
26 X. Sun, X. Qiu, L. Li and G. Li, *Inorg. Chem.*, 2008, **47,** 4146.
27 V.R. Shinde, H.S. Shim, T.P. Gujar, H.J. Kim and W.B. Kim, *Adv. Mater.*, 2008, **20,** 1008.
28 L. Xu, Y. Ding, C. Chen, L. Zhao, C. Rimkus, R. Joesten and S. Suib, *Chem. Mater.*, 2008, **20,** 308.
29 Y. Luo, G. Li, G. Duan and L. Zhang, *Nanotechnology*, 2006, **17,** 4278.
30 L. Dong, Y. Chu and W. Sun, *Chem.—Eur. J.*, 2008, **14,** 5064.
31 M. Toupin, T. Brousse and D. Belanger, *Chem. Mater.*, 2004, **16,** 3184.
32 S. Cheng, D. Yan, J. T. Chen, R. F. Zhuo, J. J. Feng, H. J. Li, H. T. Feng and P. X. Yan, *J. Phys. Chem. C*, 2009, **113,** 13630.
33 J. liang, B. dong, S. ding, C. Li, B. Q. Li, J. Li and G. Yang, *J. mater. Chem. A*, 2014, **2**, 11299.
34 W. E. Mustain and J. Prakash, *Proc. - Electrochem. Soc.*, 2003, **30,** 71.
35 X. Xu, J. Liang, H. Zhou, S. Ding and D. Yu, *RSC Adv.*, 2014, 4, 3181.
36 S. Chen, J. Zhu, X. Wu, Q. Han and X. Wang, *ACS Nano*, 2010, **4,** 2822.
37 X. Xu, H. Zhou, S. Ding, J. Li, B. Li, D. Yu, *J. Power sources*, 2014, 267, 641.
38 G. D. Sulka, V. Moshchalkov, G. Borghs and J. P. Celis, *J. Appl. Electrochem.*, 2007, **37,** 789.
39 J. Chen, N. Xia, T. Zhou, S. Tan, F. Jiang and D. Yuan, *Int. J. Electrochem. Sci.*, 2009, **4,** 1063.
40 P. Kurzweil, The 14th International Seminar On Double Layer Capacitors, Deerfield Beach, FL, U.S.A., 2004.
41 S. K. Meher, P. Justin and G. R. Rao, *Nanoscale*, 2011, **3,** 683.
42 Q. Cheng, J. Tang, J. Ma, H. Zhang, N. Shinya and L. C. Qin, *Phys. Chem. Chem. Phys.*, 2011,**13,** 17615.